Spectrochimica Acta Part A: Molecular and Biomolecular Spectroscopy 135 (2015) 241–251

Contents lists available at ScienceDirect

Spectrochimica Acta Part A: Molecular and Biomolecular Spectroscopy

journal homepage: www.elsevier.com/locate/saa

Combustion synthesized tetragonal ZrO_2: Eu^{3+} nanophosphors: Structural and photoluminescence studies

Y.S. Vidya [a], K.S. Anantharaju [b],*, H. Nagabhushana [c], S.C. Sharma [d], H.P. Nagaswarupa [b], S.C. Prashantha [b], C. Shivakumara [e], Danithkumar [c]

[a] Department of Physics, Lal Bahadur Shastry Government First Grade College, Bangalore 560 032, India
[b] Research Center, Department of Science, East West Institute of Technology, Bangalore 560 091, India
[c] Prof. C.N.R. Rao Centre for Advanced Materials Research, Tumkur University, Tumkur 572 103, India
[d] Vice Chancellor, Chhattisgarh Swami Vivekananda Technical University, North Park Avenue, Sector-8, Bhilai, Chhattisgarh 490 009, India
[e] Solid State and Structural Chemistry Unit, Indian Institute of Science, Bangalore 560 012, India

HIGHLIGHTS

- Tetragonal ZrO_2: Eu^{3+} (1–11 mol%) nanophosphors were prepared by a low temperature combustion method.
- Stable orange–red emission was observed from ZrO_2: Eu^{3+} (1–11 mol%) tetragonal phase.
- The ZrO_2: Eu^{3+} (1–11 mol%) phosphors were potential candidates in luminescence devices especially in WLEDs.

GRAPHICAL ABSTRACT

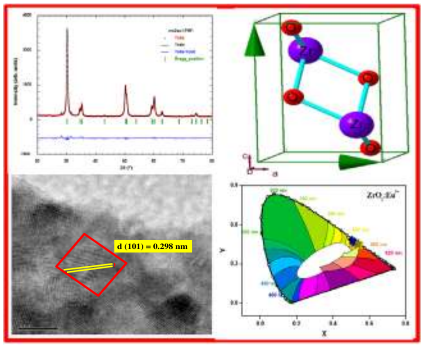

ARTICLE INFO

Article history:
Received 2 May 2014
Received in revised form 15 June 2014
Accepted 29 June 2014
Available online 9 July 2014

Keywords:
Solution combustion synthesis
ZrO_2: Eu^{3+}
Photoluminescence
Rietveld

ABSTRACT

Novel crystalline tetragonal ZrO_2: Eu^{3+} phosphors were prepared by a facile and efficient low temperature solution combustion method at 400 ± 10 °C using oxalyl dihydrazide (ODH) as fuel. The powder X-ray diffraction patterns and Rietveld confinement of as formed ZrO_2: Eu^{3+} (1–11 mol%) confirmed the presence of body centered tetragonal phase. The crystallite size estimated from Scherrer's and W–H plots was found to be in the range of 7–17 nm. These results were in good agreement with transmission electron microscopy studies. The calculated microstrain in most of the planes indicated the presence of tensile stress along various planes of the particles. The observed space group (*P4₂/nmc*) revealed the presence of cations in the *2b* positions (0.75, 0.25, 0.25) and the anions in the *4d* positions (0.25, 0.25, 0.45). The optical band gap energies estimated from Wood and Tauc's relation was found to be in the range 4.3–4.7 eV. Photoluminescence (PL) emission was recorded under 394 and 464 nm excitation shows an intense emission peak at 605 nm along with other emission peaks at 537, 592, 605 and 713 nm. These emission peaks were attributed to the transition of $^5D_0 \rightarrow {}^7F_J$ ($J = 0, 1, 2, 3$) of Eu^{3+} ions. The high ratio of Intensity of ($^5D_0 \rightarrow {}^7F_2$) and ($^5D_0 \rightarrow {}^7F_1$) infers that Eu^{3+} occupies sites with a low symmetry and without an inversion center. CIE color coordinates indicated the red regions which could meet the needs of illumination devices.

---

* Corresponding author. Mobile: +91 9164118972.
E-mail addresses: vidyays.phy@gmail.com (Y.S. Vidya), ananth.che@gmail.com (K.S. Anantharaju).

http://dx.doi.org/10.1016/j.saa.2014.06.151
1386-1425/© 2014 Elsevier B.V. All rights reserved.

Introduction

Oxide phosphors were found to be optimal candidates in field emission display (FED) and plasma display panel (PDP) devices as they were sufficiently conductive to release electric charges stored on the phosphor particle surfaces [1]. Because, these potential applications are still very much in the design phase, further fundamental research in the field remains a challenge. Among these oxide phosphors, zirconium oxide/zirconia is a material that deserves attention in the field of photonics. Zirconia was a technologically important material due to its high melting point, high thermal and mechanical resistance, high thermo chemical resistance, high thermal expansion coefficient, low thermal conductivity, high corrosion resistance, high dielectric constant, photo thermal stability *etc.* [2–5]. Most of these applications make use of size-dependent properties of zirconia nanocrystals. It was an important task to synthesize the crystallite size as small as possible. When zirconia particles are reduced to nano scale size, novel characteristics may be found due to quantum size effects, which occur when cluster size was smaller than the Bohr exaction radius [6]. Therefore, the precise control of the crystallite size, crystalline phase, morphology, textural properties and lattice defects was absolutely required [7].

Zirconia exists in three crystalline phases: monoclinic (below 1170 °C), tetragonal (1170–2370 °C) and cubic (above 2370 °C) [3,4]. Among these, tetragonal/cubic phase was most desirable for technical applications [2,8,9]. In general, the increasing temperature stabilizes more symmetric phases [10–14]. The assignment of tetragonal and cubic phase solely from the XRD can be misleading, since these two phases have similar XRD patterns [2]. The problem was more pronounced when the peaks are broadening due to small sizes of the crystals [13]. The incorporation of trivalent rare earth (RE) ions such as Y^{3+}, Pr^{3+} and Eu^{3+} promotes the formation of oxygen vacancies for charge compensation and favors sevenfold coordinated oxygen ions around the ‘Zr’ cations and stabilize tetragonal or cubic phases at low temperature [15–20]. The stabilization of the tetragonal or cubic phase from monoclinic phase is very crucial as these two phases are considered to be more important in fundamental and technological applications than the low temperature phase.

Norris et al. described the important role of the crystal phase in the efficiency of transition metal doped semiconducting nanoparticles [21]. To date, many methods have been deployed to prepare ZrO_2: Eu^{3+} luminescent phosphors in the form of powders, thin films or colloidal solutions by sol–gel method [22], polyol method [2], co-precipitation method [23] *etc.* Traditionally solid-state method was used for the preparation of phosphor materials for Solid State Lightning (SSL) applications. The conventional SSL method is (i) inhomogeneity of the final product, (ii) low-surface area, formation of large agglomerated particles and (iii) presence of various defects (surface, impurities) which are harmful to luminescence [24,25]. These problems were overcome by the use of solution combustion method [26]. This technique produces uniform product, high surface area, fine particles, lesser processing time and cost effective method.

In this communication, low temperature solution combustion synthesis was demonstrated to be a versatile and energy efficient method for preparing ZrO_2: $Eu^{3+}{}_{x\%}$ ($x = 1, 3, 5, 7, 9$ and 11 mol%) nanophosphors. The obtained nanopowders were characterized using X-ray diffraction (XRD), scanning electron microscopy (SEM), transmission electron microscopy (TEM) and UV–Visible absorption spectroscopy. In addition the effect of europium substitution on photoluminescence (PL) properties were investigated for their possible usage in lighting applications.

Experimental

The raw materials, zirconium (IV) oxynitrate hydrate ($ZrO(NO_3)_2{\cdot}xH_2O$: 99.99%, S.D. Fine Chemicals Company Ltd.) and europium oxide (Eu_2O_3: 99.99%, Merck Ltd.) are the sources of Zr and Eu respectively. Oxalyl dihydrazide (ODH: $C_2H_6N_4O_2$) was used as fuel. The stoichiometry of redox mixture used for combustion is calculated using total oxidizing and reducing valences of compounds [27].

For the synthesis of ZrO_2: Eu^{3+} (1–11 mol%), Eu_2O_3 was first converted to $Eu(NO_3)_3$ by dissolving stoichiometrically calculated amount of Eu_2O_3 in 1:1 HNO_3 and excess nitric acid was evaporated on sand bath at 80 °C to obtain transparent europium nitrate solution. Required amount of ODH and aqueous mixture of zirconium (IV) oxynitrate hydrate were subsequently added to the europium nitrate solution while continuously stirring the mixture to ensure homogeneous mixing. The petri dish containing the heterogeneous redox mixture was introduced into a muffle furnace maintained at 400 ± 10 °C. Initially the solution boils and undergoes dehydration. Eventually the mixture undergoes decomposition, which results in the liberation of large amounts of gases (usually CO_2, H_2O and N_2). This was followed by a spontaneous ignition which resulted in flame type combustion [28]. The whole process was completed in less than 5 min and a highly porous ZrO_2: Eu^{3+} nano powder was obtained.

The final products were characterized using Shimadzu Powder X-ray diffractometer (PXRD). The diffraction patterns were recorded at room temperature using Cu Kα (1.541 Å) radiation with nickel filter in the 2θ range 20–70° at a scan rate of 2° min^{-1}. The morphological features and particle size were studied by scanning electron microscopy (SEM, Hitachi-3000) and transmission electron microscopy (TEM, TECNAIF-30) respectively. The UV–Visible absorption spectrum was recorded on SL 159 EUCO UV–Visible Spectrophotometer. The PL measurements were performed on a Horiba Flurolog Spectrofluorometer at RT.

Results and discussion

Powder X-ray diffraction studies (PXRD)

Normally oxide samples require high calcination temperature to get single pure phase. Table 1 shows zirconia hosts prepared by different methods [29–35]. Several fuels urea, glycine, oxalic acid, citric acid *etc.* were employed for synthesis. Compared to other fuels, ODH has low ignition temperature, easily available, easy to handle and evolve low molecular weight, harmless gases. The oxide materials prepared by using ODH as a fuel finds variety of applications as catalysts, phosphors, pigments, refractories and SYNROC (synthetic rock) *etc.* [36,37].

Fig. 1A shows the PXRD patterns of ZrO_2: Eu^{3+} (1, 3, 5, 7, 9 and 11 mol%) nanophosphors. The as-formed ZrO_2: Eu^{3+} prepared by low temperature solution combustion technique using ODH as fuel shows pure tetragonal phase (JCPDS 81-1544) without any post calcinations and no traces of additional peaks from monoclinic/cubic phase were observed. The oxygen vacancies were considered to be responsible for the formation of the tetragonal phase. It was seen that intensity of (101) plane decreases above 5 mol% doping implying the degeneration of crystallinity at higher doping concentration. In addition, it was clearly seen that with the increase of Eu^{3+} concentration, the diffraction peak (101) of ZrO_2: Eu^{3+} samples slightly shift towards lower angle (Fig. 1B). This peak shifting and line broadening was due to the partial replacement of the smaller Zr^{4+} ions by larger Eu^{3+} ions [38].

Table 1
Calcination temperatures of pure, doped and co-doped zirconia by different authors.

Sl. No	Sample	Preparation technique	Calcination /annealing temperature	Observed phases	Reference
1	ZrO_2: Eu^{3+}	Solution combustion	Without calcination	T	Present work
2	ZrO_2: Eu^{3+}	Sol–emulsion–gel	1000 °C	M and T	Ghosh and Patra [29]
3	ZrO_2: Eu^{3+}	Templating	Dried at RT for 24 h	T	Qu et al., [34]
4	ZrO_2: Y^{3+}, Eu^{3+}	Solid state	1600 °C	M, C and T	Hui et al., [35]
5	ZrO_2: Dy^{3+}	Co-precipitation	600 °C	M and T	Giu et al., [23]
6	ZrO_2: Eu^{3+}	Hydrothermal	750° C	C	Smits et al., [33]
7	ZrO_2	Solution combustion	Without calcination	C	Prakashbabu et al., [32]
8	ZrO_2: Y^{3+}, Eu^{3+}	Sol–gel	800 °C	M and T	Liao et al., [30]
9	ZrO_2: DY^{3+}, Eu^{3+}	Wet chemical	1000 °C	M and T	Das et al., [31]

*Where M; monoclinic, T; tetragonal and C; cubic phase.

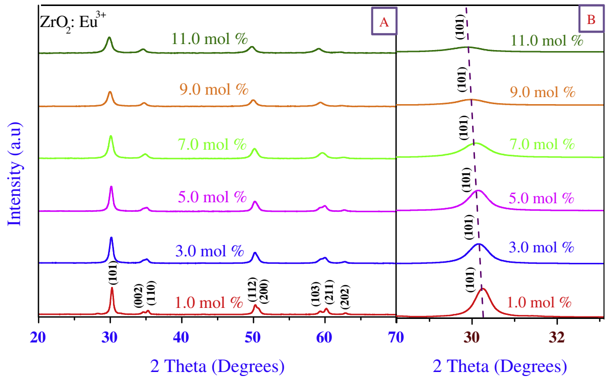

Fig. 1. (A) PXRD patterns of as-formed ZrO_2: Eu^{3+} (1–11 mol%) nanoparticles and (B) shifting of (1 0 1) XRD peak towards lower angle with increase in Eu^{3+} concentration.

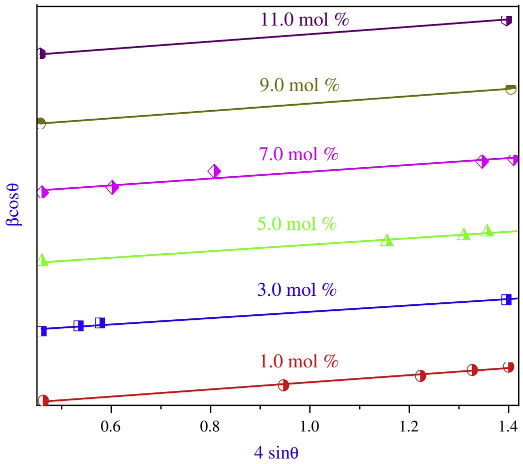

Fig. 2. W–H plots of as-formed ZrO_2: Eu^{3+} (1–11 mol%) nanoparticles.

It has been demonstrated that, with decrease in crystallite size, the crystal lattice tends to transform into a structure with more symmetrical tetragonal/cubic phase [11,14]. Therefore, to observe the variation of crystallite size with Eu^{3+} concentration in ZrO_2, Debye–Scherrer's equation and Williamson and Hall plots were employed to determine the crystallite sizes [39,40].

$$D = \frac{0.9\lambda}{\beta\cos\theta} \tag{1}$$

where 'β'; the diffracted full width at half maximum (FWHM in radian) caused by the crystallites, 'λ'; the wavelength of X-ray (1.542 Å), 'θ'; the Bragg angle and k; is the constant depends on the grain shape (0.90). It was found that the average crystal sizes estimated for ZrO_2: Eu^{3+} (1–11 mol%) were found to be in the range of 7.1–17.5 nm.

W–H plots have suggested a method combining the domain size and lattice micro-strain effects on line broadening, when both are operative [38]. The W–H approach considers the case when the domain effect and lattice deformation are both simultaneously operative and their combined effects give the final line broadening FWHM (β), which is the sum of grain size and lattice distortion. This relation assumes a negligibly small instrumental contribution compared with the sample-dependent broadening. W–H equation may be expressed in the form:

$$\beta\cos\theta = \varepsilon(4\sin\theta) + \frac{\lambda}{D} \tag{2}$$

where β (FWHM in radians) is measured for different XRD lines corresponding to different planes, ε; the strain developed and D; the grain size. The equation represents a straight line between $4\sin\theta$ (X-axis) and $\beta\cos\theta$ (Y-axis) (Fig. 2). The slope of the line gives the strain (ε) and intercept (λ/D) of this line on the Y-axis gives grain size (D). The grain size for all the Eu^{3+} doped ZrO_2 were found to be in the range of 7.2–17.8 nm. The obtained values were well comparable with that calculated from Scherrer's equation. The crystallite sizes estimated from W–H plots were slightly higher than those calculated using Scherrer's formula (Table 2). The small variation in the values were due to the fact that in Scherrer's formula strain component was assumed to be zero and observed broadening of diffraction peak was considered as a result of reducing grain size only. Strain continues to increase with increase in Eu^{3+} concentration. Garvie et al., showed the existence of a critical size of ~30 nm, below which the metastable tetragonal phase was stable in nanocrystalline ZrO_2 and above which the monoclinic phase was stable [41].

The average crystallite size estimated from both the methods were found to decrease with increase in Eu^{3+} concentration (1–11 mol%) where interstitial 'Zr' plays an important role in the grain growth of ZrO_2: Eu^{3+}. In general, the moving boundaries were attached to the 'Zr' interstitials. Gradual increase of Eu^{3+} doping progressively reduces the concentration of 'Zr' in the system. Thus the diffusivity was decreased in ZrO_2, which resulted in a suppressed grain growth of ZrO_2: Eu^{3+} samples. At the same time, the substituted Eu^{3+} ions provide a retarding force on grain boundaries. If the retarding force generated was more than the driving force for grain growth due to 'Zr', the movement of grain boundary was impeded [42]. This in turn decreases crystallite size with increasing Eu^{3+} concentration.

The other structural parameters; dislocation density (δ), microstrain (ε), stress (σ) and stacking fault (SF) are determined using the following relation [43]:

$$\delta = \frac{1}{D^2} \tag{3}$$

$$\sigma_{\text{stress}} = \frac{\text{microstrain}}{2} \times E \tag{4}$$

$$\text{SF} = \left[\frac{2\pi^2}{45(3\tan\theta)^{1/2}}\right] \tag{5}$$

Table 2
Estimated crystallite size (Scherrer's formula and W–H method), strain, dislocation density and surface factor of ZrO_2: Eu^{3+} (1–11 mol%) nanophosphors.

Samples	FWHM (rad)	Crystallite size (nm)		Strain (ε) × 10^{-3}	SF × 10^{-3}	δ (10^{15} lin m^{-2})
		Scherrer's formula	W–H plot			
ZrO_2: $Eu^{3+}_{1.0mol\%}$	0.470	17.51	17.83	7.599	3.995	3.261
ZrO_2: $Eu^{3+}_{3.0mol\%}$	0.598	13.78	14.01	9.672	5.089	5.266
ZrO_2: $Eu^{3+}_{5.0mol\%}$	0.641	12.86	13.02	10.37	5.712	6.046
ZrO_2: $Eu^{3+}_{7.0mol\%}$	0.794	10.37	10.68	12.88	6.767	9.299
ZrO_2: $Eu^{3+}_{9.0mol\%}$	0.988	08.35	08.72	16.06	8.421	14.34
ZrO_2: $Eu^{3+}_{11.0mol\%}$	1.158	07.11	07.19	18.93	9.907	19.78

where '*E*' is the elastic constant or generally known as Young's modulus of the material. Young's modulus of the zirconium oxide is 186.21 GPa [44]. Table 3 gives the interplanar distances (observed and standard), their deviations, microstrain and stress on the grains of (1 0 1) plane. The microstrain on the grains can be visualized from the line shifting in the XRD spectrum. It can be observed that the observed *d*-spacing of the diffraction planes were very close to the standard values. Therefore the Δd_{hkl} values were very small in the order of 10^{-3} nm. The deviation in the *d*-spacing was the measure of line shifting which gives the value of micro strain in the nano powder sample. If d_0 is the observed *d*-spacing of the prepared sample and d_s, the spacing in the standard sample, the micro strain in the particles in the direction normal to the diffraction plane is $\Delta d_{hkl}/d_s$. If $d_0 > d_s$, then the microstrain is positive which indicates that the residual stress is tensile and if $d_0 < d_s$, microstrain is negative indicating generation of residual compressive stress in the surface. In the present study, calculated microstrain in most of the plane is positive, indicating the presence of tensile stress on the surface of the particles.

Earlier it was reported that most of the XRD peaks of the tetragonal and cubic phase of zirconia were overlapped and it was very difficult to distinguish between the two from XRD patterns [30–32]. In order to obtain the justification regarding the tetragonal phase and the lattice parameters, Rietveld refinement analysis was carried out on ZrO_2: Eu^{3+} (1–11 mol%). The analysis was performed with the *FULLPROF* program [45,46]. The refined parameters such as occupancy, atomic functional positions for ZrO_2: Eu^{3+} (1–11 mol%) were summarized in Table 4. From Table 4, it was observed that all the ZrO_2: Eu^{3+} (1–11 mol%) shows pure tetragonal phase with lattice parameter a = 3.603–3.665 Å; c = 5.188–5.201 Å; V = 67.36–69.84 $Å^3$ and space group (*P4₂/nmc*). The cations and anions were located in the *2b* (0.75, 0.25, 0. 25) and *4d* (0.25, 0.25, 0. 45) positions respectively. A good agreement was obtained between the experimental relative intensity (observed XRD intensities) and simulated intensity (calculated XRD intensities) from the model in Fig. 3. The experimental points were plotted as dots (●) and theoretical data was shown as solid line. The difference between theoretical and experimental data was shown in the bottom line of each figure. The vertical lines represent the Bragg's allowed peaks. The refined lattice parameters (*a* and *c*) and cell volume confirms that ZrO_2: Eu^{3+} has a body-centered tetragonal structure. The change in lattice parameters were induced by the difference of ion size of Eu^{3+} (98 pm) and Zr^{4+} (84 pm). Such changes confirm that Eu^{3+} is substituting Zr^{4+} ion. By utilizing the Rietveld refinement parameters the packing diagram was drawn using Diamond software and was shown in Fig. 4. Fig. 5 show the variation of (a) crystallite size and dislocation density, (b) strain and stacking fault, (c) lattice constant and volume and (d) GOF (Goodness of Fit) defined by $GOF = \chi^2 = (R_p/R_{wp})^2$ and stress as a function of Eu^{3+} concentration in ZrO_2. The GOF was found to be decreased with increase in Eu^{3+} concentration which confirms good fitting between experimental and theoretical plots. From Fig. 5(a–d) it was observed that the lattice parameters, dislocation density, strain, stacking fault and tensile stress increased with increase in Eu^{3+} concentration. This suggests the dislocations were mainly concentrated on the grain boundaries which promote the grain boundary relaxation. High defect density in the sample involving dislocations and vacancies, easily gliding and moving along grain boundaries can develop tensile stress.

Transmission electron microscopy (TEM)

The structural information of the as-formed ZrO_2: Eu^{3+} nanophosphors were further investigated by the TEM, high resolution TEM (HRTEM) and Selected Area Electron Diffraction (SAED). Fig. 6 represents the TEM image of ZrO_2: Eu^{3+} (3 mol%). Morphological observation by TEM (Fig. 6a) indicates that the ZrO_2: Eu^{3+} consisted of aggregated nanoparticles. The average crystallite size of ZrO_2: Eu^{3+} nanophosphor was about 10 nm, which is in good agreement with the size estimated by Scherrer's equation from the XRD pattern. Fig. 6b shows the SAED pattern from ZrO_2: Eu^{3+} nanophosphors. The observed diffraction rings in SAED pattern clearly indicate high crystallinity of the sample. These diffraction rings were indexed to (1 0 1), (1 1 0), (1 1 2) and (2 1 1) planes which were attributed to tetragonal phase of ZrO_2: Eu^{3+}. Combining with the high resolution TEM image (HRTEM) (Fig. 6c), it can be clearly seen that the lattice fringes with the interplanar spacing of 0.296 nm corresponds to the distance of the (1 0 1) plane of the tetragonal structure of ZrO_2: Eu^{3+}, which suggests that high quality tetragonal nanocrystals were formed in ZrO_2: Eu^{3+}. In HRTEM, there was no evidence for the presence of Eu_2O_3 crystalline phase on the nanoparticles, confirming that Eu^{3+} ions remain within the crystalline lattices. This can be clearly observed in EDS spectrum (Fig. 6d) of the ZrO_2: Eu^{3+} (3.0 mol%), which shows the presence of Zr, O and

Table 3
Interplanar d_{hkl} spacing, micro strain and stress in t-ZrO_2: Eu^{3+} (1–11 mol%) nanophosphors.

ZrO_2: Eu^{3+} (mol%)	Interplanar spacings of (1 0 1) plane		Deviation $\Delta d = d_o - d_s$ (nm)	$\varepsilon = \Delta d/d_s$	σ_{stress} (MPa)
	d_{obs} (nm)	d_{std} (nm)			
1	2.963	2.9591	0.0039	0.0013	121.03
3	2.9615	2.9591	0.0024	0.0081	754.15
5	2.9731	2.9591	0.014	0.0047	437.59
7	2.9750	2.9591	0.0156	0.0053	490.66
9	2.9750	2.9591	0.0159	0.0054	499.91
11	2.9945	2.9591	0.0354	0.0112	1024.4

Table 4
Rietveld refined structural parameters for ZrO_2:Eu^{3+} (1–11 mol%) nanophosphors.

Compounds	ZrO_2: $Eu_{1mol\%}$	ZrO_2: $Eu_{3mol\%}$	ZrO_2: $Eu_{5mol\%}$	ZrO_2: $Eu_{7mol\%}$	ZrO_2: $Eu_{9mol\%}$	ZrO_2: $Eu_{11mol\%}$
Crystal system	Tetragonal	Tetragonal	Tetragonal	Tetragonal	Tetragonal	Tetragonal
Space group	*P42/nmc* (*137*)	*P42/nmc* (*137*)	*P42/nmc* (*137*)	*P42/nmc* (*137*)	*P42/nmc* (*137*)	*P42/nmc* (*137*)
Lattice parameters (Å)						
a	3.603(2)	3.612(7)	3.629(5)	3.613(7)	3.649(3)	3.665(3)
c	5.188(6)	5.181(9)	5.175(9)	5.182(9)	5.168(9)	5.201(8)
Unit cell volume (Å^3)	67.36(2)	67.58(3)	68.14(5)	67.65(3)	68.80(9)	69.84(3)
Atomic coordinates						
Zr/Eu	(2b)	(2b)	(2b)	(2b)	(2b)	(2b)
x	0.7500	0.7500	0.7500	0.7500	0.7500	0.7500
y	0.2500	0.2500	0.2500	0.2500	0.2500	0.2500
z	0.2500	0.2500	0.2500	0.2500	0.2500	0.2500
O	(4d)	(4d)	(4d)	(4d)	(4d)	(4d)
x	0.25	0.25	0.25	0.25	0.25	0.25
y	0.25	0.25	0.25	0.25	0.25	0.25
z	0.4509(9)	0.4495(3)	0.4420(3)	0.4488(8)	0.4351(3)	0.4213(6)
$R_{Factors}$						
R_P	3.60	2.47	2.11	2.28	2.02	1.87
R_{WP}	5.24	3.09	2.67	2.87	2.57	2.35
R_{Exp}	6.44	6.33	5.89	6.28	7.60	7.17
χ^2	0.66	0.24	0.21	0.21	0.12	0.11
R_{Bragg}	2.21	2.22	1.96	2.20	2.82	2.87
R_F	3.23	3.24	2.73	2.86	3.46	3.25

Eu elements. Combining with XRD analysis above, these results further confirm that Eu^{3+} has been effectively built into the ZrO_2 host lattice.

Scanning electron microscopy (SEM)

The SEM micrographs of ZrO_2: Eu^{3+} (3.0 mol%) nanophosphor show the crystallites with irregular shape and contain several voids and pores (shown in the form of circles) because of the escaping gases during combustion synthesis (Fig. 7). It can be observed that the crystallites have no uniform shape and size. This was believed to be related to the non-uniform distribution of temperature and mass flow in the combustion flame. This type of porous network is a typical characteristic of combustion synthesized powders. The porous powders are highly friable which facilitates easy grinding to obtain finer particles. When the gas is escaping with high pressure pores are formed with the simultaneous formation of small particles near the pores [47].

UV–Visible absorption spectrum and optical energy gap (E_g)

The UV–Visible absorption spectra of ZrO_2: Eu^{3+} (1–11 mol%) nanomaterials in the wavelength range 200–800 nm was shown in Fig. 8. The spectra shows strong and prominent absorption band with maximum at around 214 nm which could arise due to transition between valence band to conduction band [31]. The weak absorption in the UV–Visible absorption region was expected to arise from transitions involving extrinsic states such as surface traps/defect states/impurities [48]. Smaller sized particles were found to have high surface to volume ratio. This results in increase of defects distribution on the surface of nanomaterials. Thus if the particle size is small; nanomaterials exhibit strong and absorption bands [49]. In ZrO_2: Eu^{3+}, the particle size was in nanometer which results in high surface to volume ratio as a result, there is an increase in defects distribution on the surface of the nanomaterials.

For estimation of band gap in the nanomaterials, the absorbance spectra of ZrO_2: Eu^{3+} (1–11 mol%) nanophosphors in transmission mode were recorded by distributing the particles uniformly in liquid paraffin, in the wavelength range of 200–800 nm. For a direct band gap, the absorption coefficient near the band edge was given by Wood and Tauc's relation [50].

$$\alpha = \frac{A}{h\nu}(h\nu - E_g)^{1/2} \tag{6}$$

where *a*; absorption co-efficient, $h\nu$; the photon energy, E_g; the energy gap and *A*; the constant depending on the type of transition. From the Eq. (6) $\alpha h\nu = 0$, $E_g = h\nu$. The energy gap is determined by plotting $(\alpha h\nu)^2$ versus $h\nu$ and finding the intercept on the '$h\nu$' axis by extrapolating the plot to $(\alpha h\nu)^2 = 0$. Inset of Fig. 8 shows the Wood and Tauc plot from which the direct band gap is obtained in the range of 4.3–4.7 eV. The optical energy band gap was found to decrease with decrease in crystallite size or increase in Eu^{3+} concentration. This band gap narrowing was primarily attributed to the substitutional RE ions. Some electronic states were introduced into the band gap of ZrO_2 by RE *4f* electrons, which were located close to the lower edge of the conduction band to form the new lowest unoccupied molecular orbital. Consequently, the absorption edge transition for the ZrO_2: Eu^{3+} takes from *2p* level of oxygen to *4f* level of RE ions.

Photoluminescence (PL) studies

Among the various RE elements incorporated in zirconia, Eu^{3+} is generally employed in telecommunications, displays and luminescent devices [51–53]. The splitting of Eu^{3+} energy levels will be different in monoclinic, tetragonal and cubic symmetry. Higher symmetry leads to degeneration, while lower symmetry removes the degeneracy and leads to the observation of additional spectral lines [54].

Fig. 9 presents the RT excitation spectra of ZrO_2: Eu^{3+} (1–11 mol%) phosphors by monitoring the emission at 605 nm. The excitation spectrum of ZrO_2: Eu^{3+} can be divided into two regions: the excitation band extending up to ~360 nm is attributed to the charge transfer transitions of Eu–O group, and the narrow peaks located at wavelength longer than ~360 nm can be assigned to the *f–f* transitions of Eu^{3+}. The *f–f* transitions of Eu^{3+} in excitation spectrum include sharp lines $^7F_0 \rightarrow {}^5L_6$ (Eu^{3+}) at ~394 nm and $^7F_0 \rightarrow {}^5D_2$ (Eu^{3+}) at ~464 nm [55]. Among these excitation transitions, $^7F_0 \rightarrow {}^5L_6$ (394 nm) is the most intense peak, which matches well with the commercially available near-UV GaN-based LED chips [38].

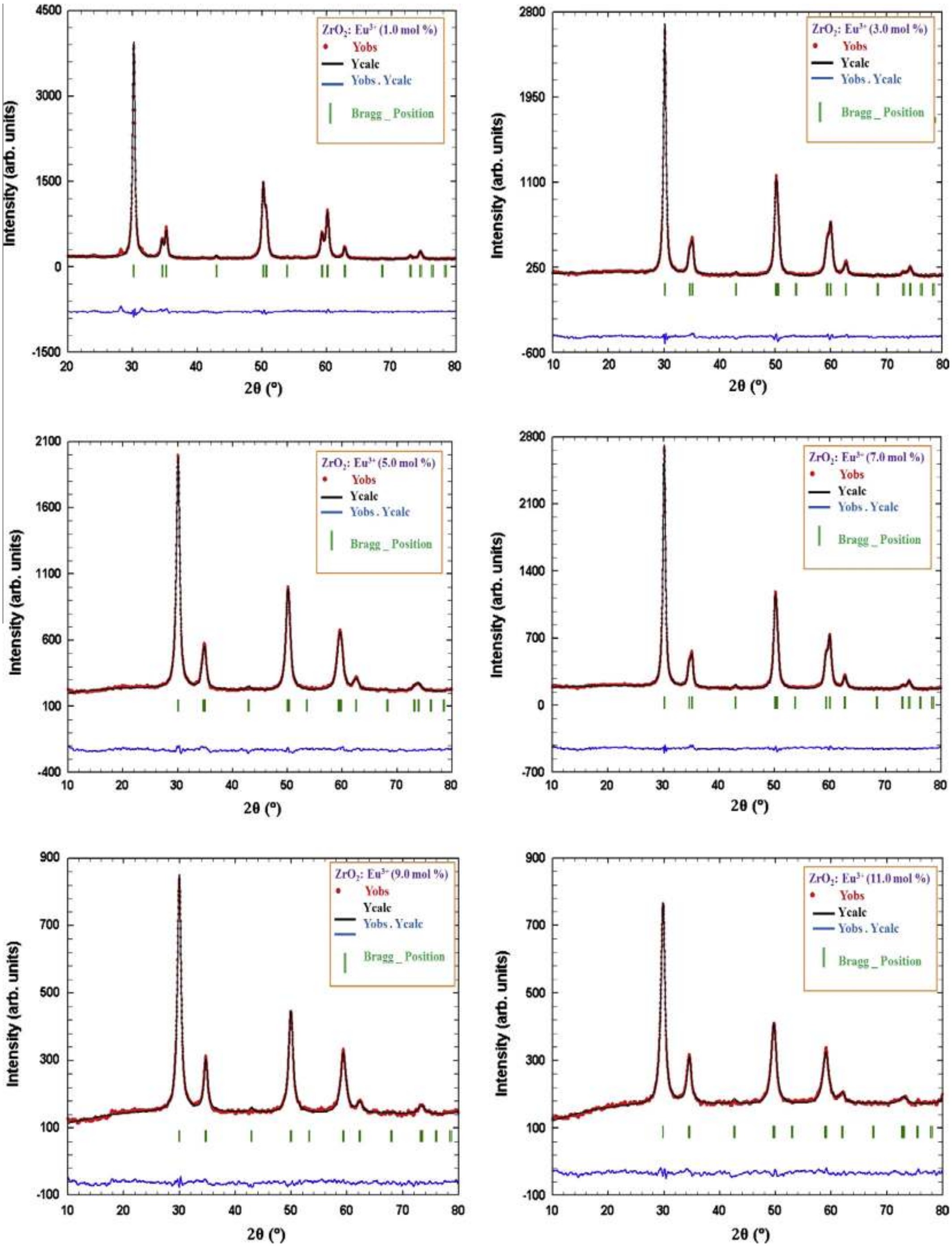

Fig. 3. Rietveld refinement of as-formed tetragonal ZrO_2: Eu^{3+} (1–11 mol%) nanophosphors.

Figs. 10a and b shows the emission spectra of ZrO_2: Eu^{3+} (1–11 mol%) at both 394 and 464 nm excitation respectively. All spectra were taken under identical conditions. The PL measurements for two excitations indicated no significant change in the emission shape of position except PL intensity. The emission spectra consist of peaks located in the wavelength range from 500 to 760 nm. These peaks correspond to transitions from the $^5D_0$ state to the ^7F_J ($J = 0, 1, 2, 3, 4$) state of the $^4f_6$ configuration of Eu^{3+}. It is well known that the $^5D_0 \rightarrow {}^7F_2$ lines of Eu^{3+} are of electric-dipole (ED) nature and very sensitive to site symmetry, while the $^5D_0 \rightarrow {}^7F_1$ lines are primarily magnetic dipole in nature. The intensity distribution of the $^5D_0 \rightarrow {}^7F_J$ transitions among different J ($J = 0, 1, 2, 3, 4$) levels depends on the symmetry of the local environment around Eu^{3+} ions and can be described in terms of Judd–Ofelt of magnetic-dipole (MD) nature and insensitive to site symmetry theory [38,56,57]. According to selection rules, magnetic dipole transition is permitted and electric dipole is forbidden, but for some cases in which local symmetry of the activators without an inversion center, the parity forbidden is partially permitted, such as Eu^{3+} ion occupying C_2 sites in Y_2O_3: Eu^{3+} [58].

The emission intensity ratio between $^5D_0 \rightarrow {}^7F_2$ (605 nm) and $^5D_0 \rightarrow {}^7F_1$ (592 nm) transitions is called as asymmetric ratio is a good measure of the degree of distortion from inversion symmetry of the local environment surrounding the Eu^{3+} ions in the host

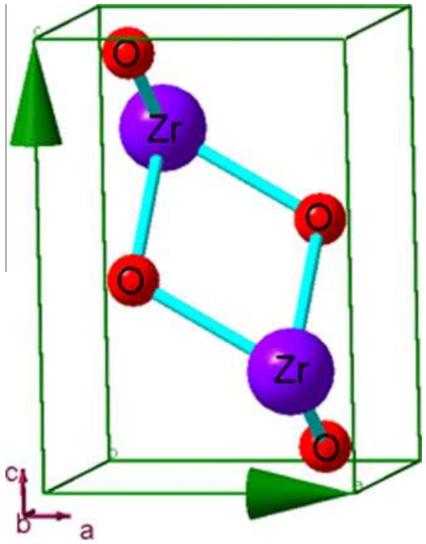

Fig. 4. Packing diagram of as-formed ZrO_2: Eu^{3+} (3.0 mol%) nanophosphor.

matrix. It can be clearly observed from the Fig. 11, that the ratio of I ($^5D_0 \rightarrow {}^7F_2$)/I ($^5D_0 \rightarrow {}^7F_1$) remains almost constant for both 394 and 464 nm excitations. The results imply that the introduction of Eu^{3+} into ZrO_2 mainly located in sites with inversion symmetry. In ZrO_2: Eu^{3+} materials, some Zr^{4+} ions are replaced by Eu^{3+} ions.

Owing to the different charge for the cations, oxygen vacancies were formed to balance the charge difference. The defect reaction equation can be described in the following Eq. (7):

$$(1-x)ZrO_2 + 1/2xEu_2O_3 = xEu'_{Zr} + 1/2xV''_o + (1-x)Zr^x_{Zr} + (2 - 1/2x)O^x_o \tag{7}$$

where Eu_{Zr}, means Eu^{3+} occupying the normally occupied by a Zr^{4+} due to replacement by Eu^{3+}. V_o'' is the O^{2-} vacancy. $Zr_{Zr}{}^x$ represents the rest zirconium in the lattice of ZrO_2 and $O_o{}^x$ is the oxygen in the lattice of ZrO_2. At low concentrations (x = 1 mol%), there is little V''_o in ZrO_2, and the symmetry of the host structure is not seriously influenced. The larger the concentration of Eu (x) in the host, higher the number of 'O' vacancies is able to create a new surrounding in the host. The new surrounding disturbs the symmetry of the host. With increase of the Eu^{3+} doping concentration, more and more Eu^{3+} ions occupy the sites with a low symmetry and without an inversion center, leading to a predominant $^5D_0 \rightarrow {}^7F_2$ ED transition in the emission spectra.

Fig. 12 shows the dependences of red emission $^5D_0 \rightarrow {}^7F_2$ (605 nm) on the Eu^{3+} doping concentration in the as-formed ZrO_2: Eu^{3+} (1–11 mol%), excited under 394 nm were compared. It was obviously seen that maximum emission intensity of the ZrO_2: Eu^{3+} phosphor appears at 3.0 mol%. When the Eu^{3+} doping concentration was higher than 3.0 mol%, the luminescence intensity reduces contrarily owing to the concentration quenching effect. The dopant concentration that determines the average distance between the two neighboring activator ions has a great impact on the PL efficiency in RE^{3+} ions doped nano crystals [59]. High doping concentrations of Eu^{3+} ions in ZrO_2 nanocrystals may bring about deleterious cross relaxations between the adjacent Eu^{3+} ions, resulting in the quenching of excitation energy and there by weak luminescence of Eu^{3+} [60]. Therefore, the optimum dopant concentration of Eu^{3+} in ZrO_2: Eu^{3+} phosphor was about 3.0 mol%. The concentration quenching occurs due to the energy transfer from one activator to the neighboring ion. The critical distance for energy transfer (R_c) in ZrO_2: Eu^{3+} was estimated

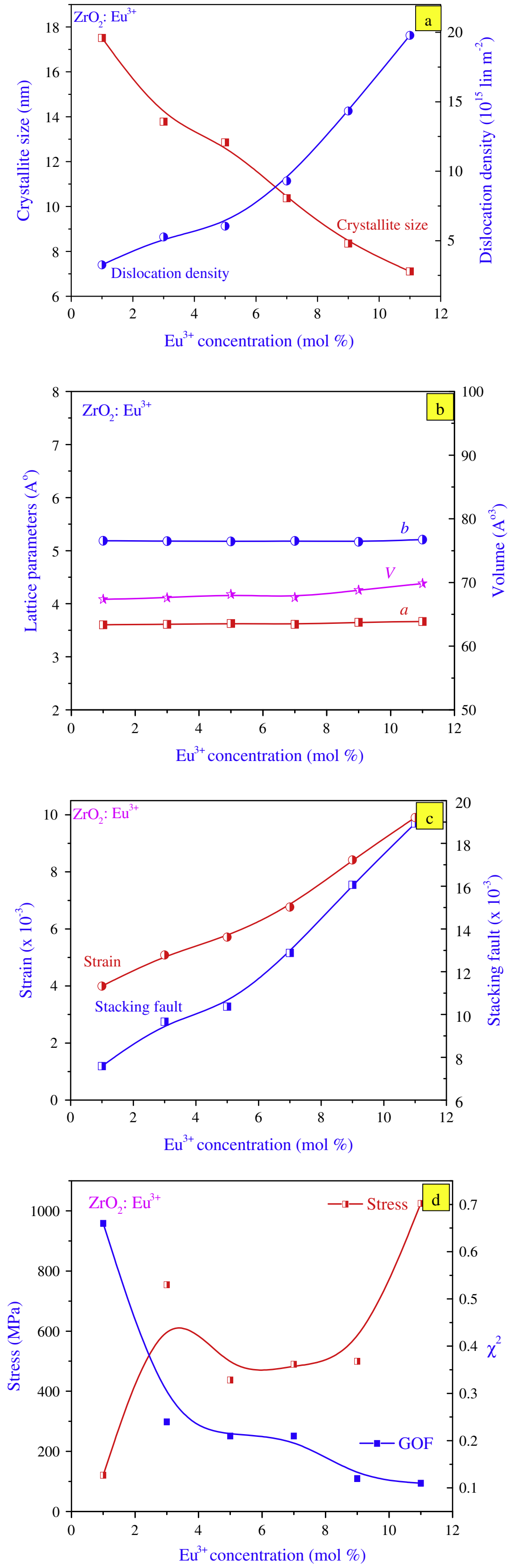

Fig. 5. The variation of (a) crystallite size and dislocation density, (b) lattice constant and unit cell volume, (c) strain and stacking fault and (d) GOF (Goodness of Fit) and stress as a function of Eu^{3+} concentration in ZrO_2.

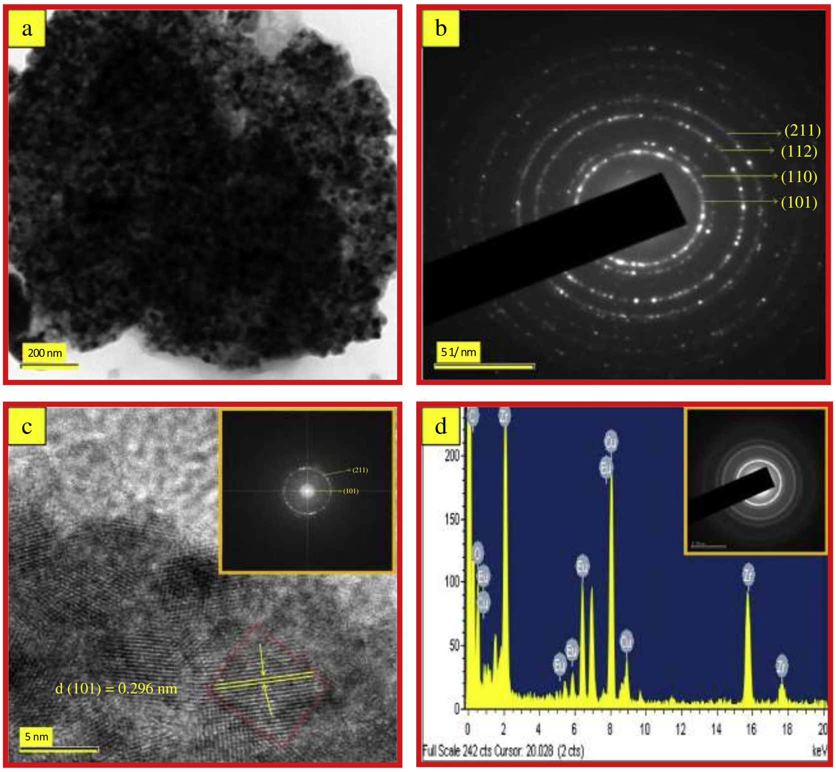

Fig. 6. TEM and HRTEM images of as-formed ZrO_2: Eu^{3+} (3.0 mol%).

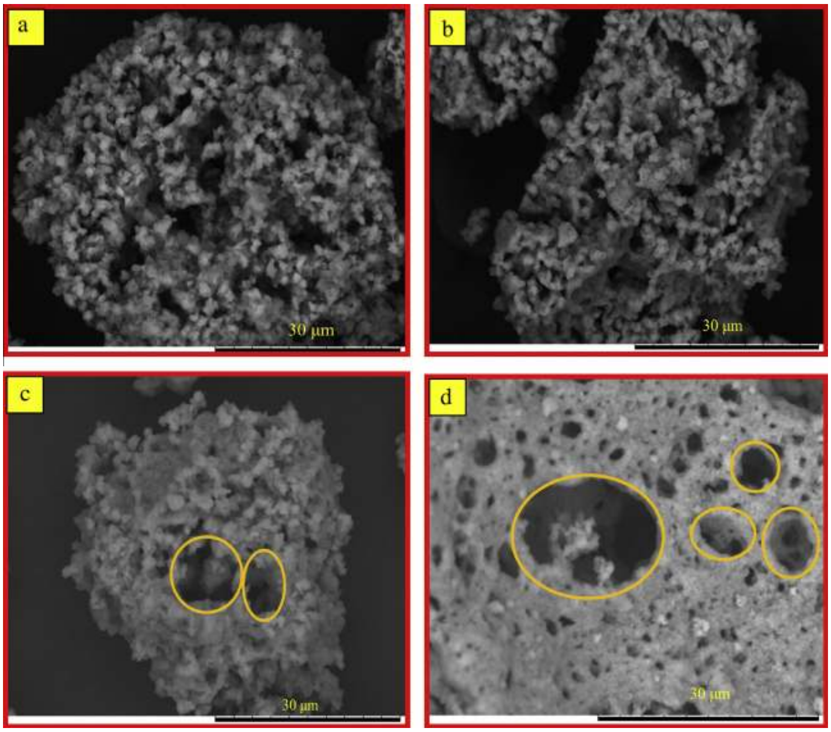

Fig. 7. Scanning electron microscopy analysis of as-formed ZrO_2: Eu^{3+} (3.0 mol%) nanophosphor.

from the structural parameters namely unit cell volume (V), total Eu^{3+} sites per unit cell (N) and critical concentration (X_c) [61].

$$R_c \approx 2\left[\frac{3V}{4X_c\pi N}\right]^{1/3} \quad (8)$$

For the ZrO_2: Eu^{3+} system, $N = 4$, $V = 67.58$ (Å)^3 and $X_c = 0.03$. The R_c of Eu^{3+} ions in ZrO_2 were found to be ~10.245 Å. When critical energy distance between Eu^{3+} ion in ZrO_2 is greater than 5 Å, the overlapping between excitation and emission spectra decreases. The energy transfer between Eu^{3+} ion take places due

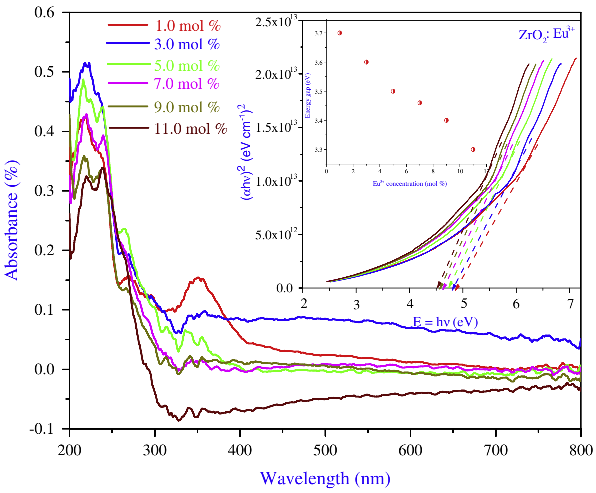

Fig. 8. UV–Visible absorption spectrum of as-formed ZrO_2: Eu^{3+} (1–11 mol%) nanoparticles. Inset: Wood and Tauc's plot to find band gap and the variation of band gap with Eu^{3+} concentration.

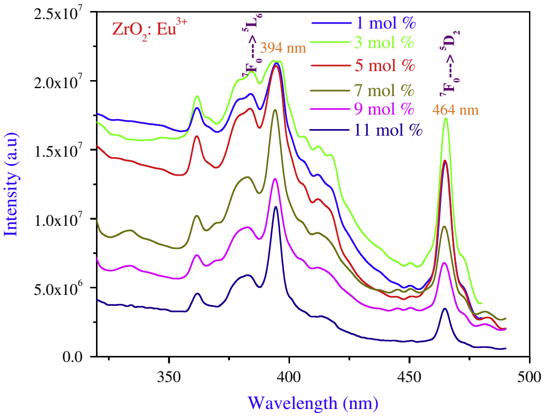

Fig. 9. Excitation spectra of as-formed ZrO_2: Eu^{3+} (1–11 mol%) nanophosphor.

to electric multipolar interaction which can be determined by the equation:

$$\frac{1}{X} = k\left[1 + \beta(X)^{Q/3}\right]^{-1} \tag{9}$$

where X; Eu^{3+} ion concentration, k and β; constants, Q = 6, 8 and 10 for dipole–dipole, dipole–quadrupole and quadrupole–quadrupole interactions. The value of Q is determined by plotting log (X) versus log ($1/X$) (Fig. 13) which gives a linear graph having a slope = −0.77 and intercept = 6.322. The Q value is close to 6 indicates that the concentration quenching in ZrO_2 is due to dipole–dipole interaction [47].

Fig. 14 shows the energy level diagram of Eu^{3+} ions and indicates possible pathways involved in this process. When the sample was excited at 394 nm wavelength, Eu^{3+} ion was raised to $^5L_6$ level from the ground state. During the emission, Eu^{3+} ion decays step wise from $^5L_6$ to $^5D_0$ level giving small quanta of energy to the lattice; it decays non-radiatively between $^5L_6$ and $^5D_0$ state. During emission, Eu^{3+} ion decays stepwise from $^5L_6$ to $^5D_0$ level. Since, the separation between $^5D_0 \rightarrow {}^7F_J$ (J = 0, 1, 2, 3, 4) is large, the step wise decay process stops here and returns to ground state by giving emission in the orange and red regions [62].

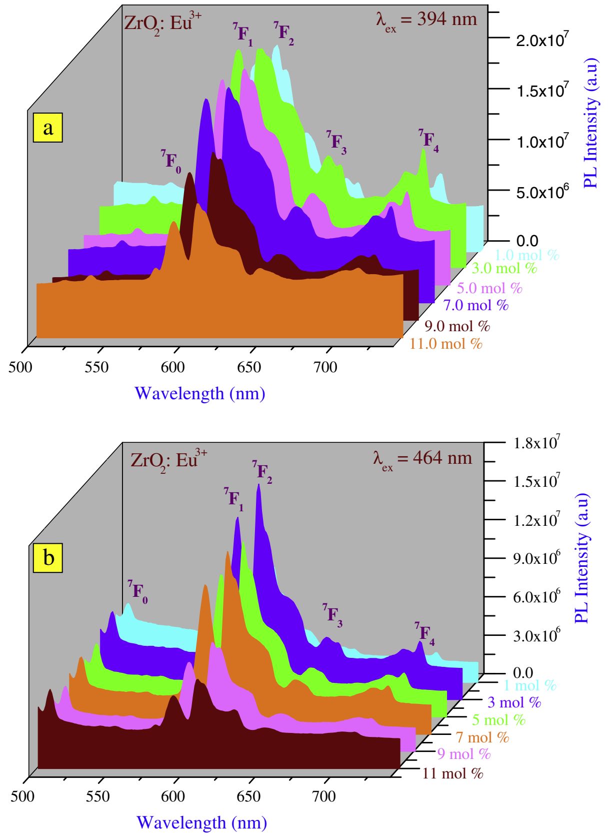

Fig. 10. PL emission spectrum of as-formed ZrO_2: Eu^{3+} (1–11 mol%) nanoparticles excited at (a) 394 nm and (b) 464 nm respectively.

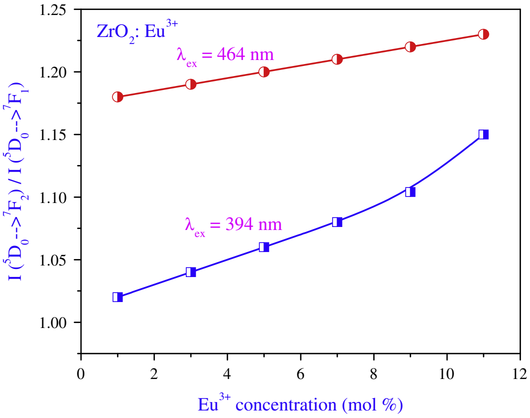

Fig. 11. The dependence of emission intensity ratio I ($^5D_0 \rightarrow {}^7F_2$)/I ($^5D_0 \rightarrow {}^7F_1$) with the Eu^{3+} doping concentration under the excitation of 394 and 464 nm.

The Commission International De I-Eclairage (CIE) 1931 chromaticity coordinates for ZrO_2: Eu^{3+} (1–11 mol%) phosphors as a function of Eu^{3+} concentration for the luminous color is depicted by the PL spectra. The CIE chromaticity coordinates calculated from the PL spectra are shown in Fig. 15. The CIE coordinates of red emission of Eu^{3+} ions not only depends upon the asymmetric ratio but also depend upon the higher energy emission levels [63]. The Eu^{3+} doping effect becomes stronger in the case of particles with higher crystallinity, resulting in improved activation energy. Interestingly, the ZrO_2: Eu^{3+} phosphor, the PL color has been modulated from yellow to red region as the Eu^{3+} content increases from 1 to

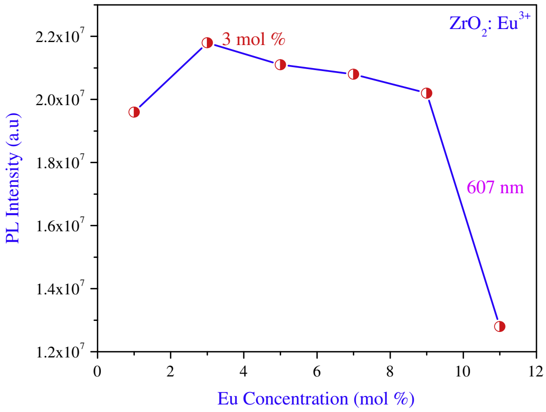

Fig. 12. Variation of PL intensity with Eu^{3+} concentration in as-formed ZrO_2 nanoparticles.

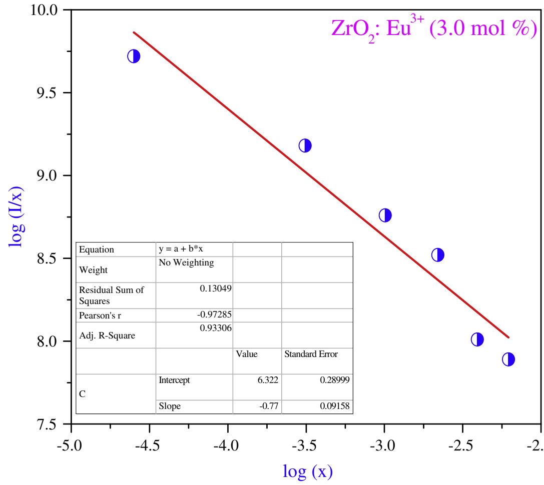

Fig. 13. Relation between log (*X*) and log (1/*X*).

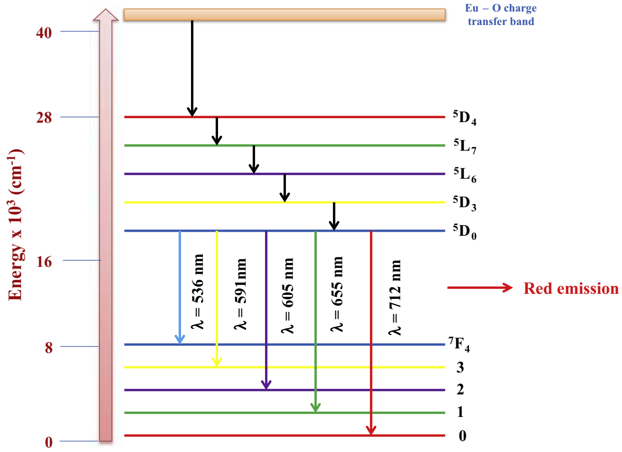

Fig. 14. The energy level diagram of Eu^{3+} ion showing the states involved in the luminescence process and the transition probabilities.

11 mol%. The color coordinates for different *Y* concentrations was given in Table 5. It is clear from the table that, the highest chromaticity coordinate values is found to be $x = 0.\ 548$, $y = 0.448$ for orange red. Further, the result indicates that emission color of

Table 5
CIE chromaticity coordinates of ZrO_2: Eu^{3+} (1–11 mol%) nanophosphor.

Eu^{3+} concentration (mol%)	*x*	*y*
1	0.518	0.465
3	0.539	0.448
5	0.548	0.441
7	0.543	0.446
9	0.536	0.451
11	0.505	0.478

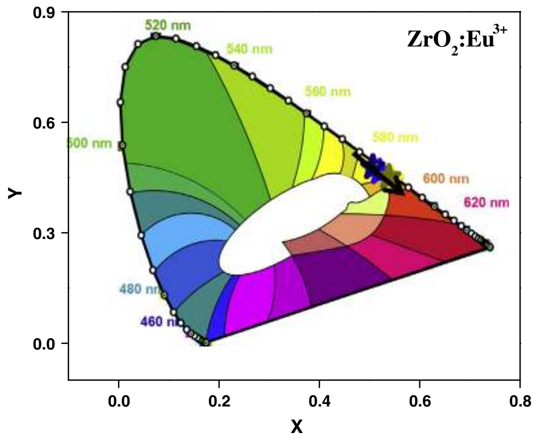

Fig. 15. The CIE chromaticity diagram of ZrO_2: Eu^{3+} (1–11 mol%) nanophosphors.

phosphors can be tuned by varying the *Y* concentrations. Therefore, the present material would be potential candidate as red phosphor in LED applications to meet the needs of illumination devices.

Conclusions

The stabilized tetragonal ZrO_2 can be successfully obtained via the low temperature solution combustion method by introducing Eu^{3+} which may have potential applications in technological fields. The particle sizes of the prepared phosphors calculated from Scherer's equation and W–H method were observed to be in the range 7–17 nm. Both crystallite size and phase composition obtained from XRD results and Rietveld refinement analyses were mirrored in TEM and HRTEM. Detailed PL studies of the ZrO_2: Eu^{3+} nanophosphors as a function of Eu^{3+} content demonstrated that the dopant concentration and the site symmetry play an important role in the emissive properties of the luminescent centers. The phosphor exhibits different emission in the range 550–750 nm due to Eu^{3+} transitions upon 394 and 464 nm excitations. It was observed that the emission spectrum excited at 394 nm showed prominent spectral lines with higher order of intensity compared to 464 nm excitation wavelengths owing to efficient energy transfer takes place from host to Eu^{3+} ions and was close to visible region which may be useful for LED applications. Further, the phosphor showed excellent CIE chromaticity coordinates (*x*, *y*) as a result, it is quite useful for display applications.

Acknowledgement

One of the author HN thanks to DST nano mission for sanctioning the research project to Center for Nano Research, Tumkur University, Tumkur for extended to carry out this research work. The authors KSA, HPN and SCP thanks to VGST, Govt. of Karnataka, India, (No: VGST/CISEE/2012-13/282) and (VGST/P-5/TRIP/2013-14) for sanctioning the research project.

References

[1] H. Zhang, X. Fu, S. Niu, Q. Xin, J. Non Cryst. Solids 354 (2008) 1559–1563.

[2] S.D. Meetei, Sh.D. Singh, V. Sudarshan, J. Alloys Compd. 514 (2012) 174–178.

[3] R. Gillani, B. Ercan, A. Qiao, T.J. Webster, Int. J. Nanomed. 5 (2010) 1–11.

[4] Y.Al. Khatatbeh, K.K.M. Lee, B. Kiefer, Phys. Rev. B 81 (2010) 214102.

[5] H.D.E. Harrison, N.T. Mclamed, E.C. Subbarao, J. Electrochem. Soc. 110 (1963) 8–23.

[6] A.A. Khosravi, M. Kundu, B.A. Kuruvilla, Appl. Phys. Lett. 67 (1995) 2506–2508.

[7] F. Gu, M.K. Lu, S.F. Wang, Y.X. QI, C.F. Song, G.J. Zhou, D. Xu, D.R. Yuan, Appl. Phys. A 78 (2004) 1059–1061.

[8] B.J. Lopez, V.D.L. Luz, F. Gonell, E. Cordonicillo, M.L. Haro, J.J. Calvino, P. Escribano, J. Alloys Compd. 519 (2012) 29–36.

[9] L. Chen, Y. Liu, Y. Li, J. Alloys Compd. 381 (2004) 266–271.

[10] K. Kuratani, M. Mizuhata, A. Kajinami, S. Deki, J. Alloys Compd. 408 412 (2006) 711–716.

[11] B.K. Moon, I.M. Kwon, J.H. Jeong, C.K. Kim, S.S. Yi, P.S. Kim, H. Choi, J.H. Kim, J. Lumin. 122 123 (2007) 855–857.

[12] A. Benyagoub, Phys. Rev. B 72 (2005) 094114.

[13] J. Joo, T. Yu, Y.W. Kim, h.M. Park, F. Wu, J.Z. Zhang, T. hyeon, J. Am. Chem. Soc. 125 (2003) 6553–6557.

[14] P. Ayyub, V.R. Palkar, S. Chattopadhyay, M. Multani, Phys. Rev. 851 (1995) 6135–6138.

[15] M.R.N. Soares, M.J. Soares, A.J.S. Fernandes, L. Rino, F.M. Costa, T.J. Monteiro, J. Mater. Chem. 21 (2011) 15262–15265.

[16] F.R. Brito, C.A. Armenta, M.G. Hipolito, E. Camarillo, A.J. Hernandez, S.H. Murrieta, C. Falcony, Opt. Mater. 30 (2008) 1840–1847.

[17] M.C. Carcoache, P.C. Rivas, A.P. Pasquevich, A.R.I. Garcia, J. Mater. Res. 8 (1993) 605–607.

[18] D.J. Kim, H.J. Jung, J. Am. Ceram. Soc. 43 (1960) 234–239.

[19] G. Morell, R.S. Katiyar, D. Torres, S.E. Paje, J. Llopis, J. Appl. Phys. 81 (1997) 2830–2834.

[20] F.A. Mumpton, R. Roy, J. Am. Ceram. Soc. 76 (1993) 2157–2160.

[21] S.C. Erwin, L. Zu, M.I. Haftel, A.L. Efros, T.A. Kennedy, D. Norris, J. Nat. 43 (2005) 91–94.

[22] L.A.D. Torres, O. Meza, D. Solis, P. Salas, E. De la Rosa, Opt. Laser Eng. 49 (2011) 703–708.

[23] F. Giu, S.F. Wang, M.K. Lu, G.J. Zhou, S.W. Liu, D. Xu, D.R. Yuan, Chem. Phys. Lett. 380 (2003) 185–189.

[24] Y.C. Kang, S.B. Park, Mater. Res. Bull. 35 (2000) 1143–1151.

[25] C.J. Shilpa, N. Dhananjaya, H. Nagabhushana, S.C. Sharma, C. Shivakumara, K.H. Sudheerkumar, B.M. Nagabhushana, R.P.S. Chakradhar, Spectrochem. Acta A 128 (2014) 730–739.

[26] K.C. Patil, M.S. Hegde, T. Rattan, S.T. Aruna, Chemistry of Nanocrystalline Oxide materials, Combustion Synthesis, Properties and Applications, World Scientific Publishing Co. Pvt. Ltd., Singapore, 2008.

[27] J.J. Kingsley, K.C. Patil, Mater. Lett. 6 (1988) 427–432.

[28] R. Ianos, I. Lazau, C. Pacurariu, P. Barvinschi, Mater. Res. Bull. 43 (2008) 3408–3415.

[29] P. Ghosh, A. Patra, Langmuir 22 (2006) 6321–6327.

[30] J. Liao, D. Zhou, B. Yang, R. Liu, Q. Zhang, Opt. Mater. 35 (2012) 274–279.

[31] S. Das, C.Y. Yang, C.h. Lu, J. Am. Ceram. Soc. 96 (2013) 1602–1609.

[32] D. Prakashbabu, R. Harikrishna, B.M. Nagabhushana, H. Nagabhushana, C. Shivakumara, R.P.S. Chakradhar, H.B. Ramalingam, S.C. Sharma, R. Chandramohan, Spectrochim. Acta, Part A 122 (2014) 216–222.

[33] K. Smits, L. Grigorjeva, D. Millers, A. Sarakovskis, A. Opalinska, J.D. Fidelus, W. Lojkowski, Opt. Mater. 32 (2010) 827–831.

[34] X. Qu, H. Song, G. Pan, X. Bai, B. Dong, H. Zhao, Q. Dai, H. Zhang, R. Qin, S. Lu, J. Phys. Chem. C 113 (2009) 5906–5911.

[35] Y. Hui, Yu Zhao, S. Zhao, L. Gu, X. Fan, L. Zhu, B. Zou, Y. Wang, J. Alloys Compd. 573 (2013) 177–181.

[36] S.T. Aruna, K.C. Patil, J. Mater. Synth. Process 4 (1996) 175–179.

[37] M. Muthuraman, N.A. Dhas, K.C. Patil, J. Mater. Synth. Process. 4 (1996) 115–120.

[38] P. Mohanty, B. Kim, J. Park, Mater. Sci. Eng. B 138 (2007) 224–227.

[39] P. Klug, L.E. Alexander, X- ray Diffraction Procedure, Wiley, New York, 1954.

[40] S.B. Qadri, J.P. Yang, E.F. Skelton, B.R. Ratan, Appl. Phys. Lett. 70 (1997) 1020–1021.

[41] R.C. Gravie, J. Phys. Chem. 69 (1965) 1238–1243.

[42] S.K. Neogi, S. Chattopadhyay, A. Banerjee, S. Bandyopadhyay, A. Sarkar, R. Kumar, J. Phys.: Condens. Matter 23 (2011) 205801.

[43] R. Suresh, V. Ponnuswamy, R. Mariappan, Appl. Surf. Sci. 273 (2013) 457–464.

[44] R.S. Lima, A. Kucuk, C.C. Berndt, Surf. Coat. Technol. 135 (2001) 166–172.

[45] S. Roy, J. Ghose, Mater. Res. Bull. 35 (2000) 1195–1203.

[46] R. Harikrishna, B.M. Nagabhushana, H. Nagabhushana, R.P.S. Chakradhar, R. Sivaramakrishna, C. Shivakumara, Tiju Thomas, J. Alloys Compd. 585 (2014) 129–137.

[47] H. Nagabhushana, B.M. Nagabhushana, M.M. Kumar, Chikkahanumantharayappa, K.V.R. Murthy, C. Shivakumara, R.P.S. Chakradhar, Spectrochim. Acta, Part A 78 (2011) 64–69.

[48] H.Q. Cao, X.Q. Qiu, B. Luo, Y. Liang, Y.H. Zhang, R.Q. Tan, M.J. Zhao, Q.M. Zhu, Adv. Funct. Mater. 14 (2004) 243–246.

[49] A. Emeline, G.V. Kataeva, A.S. Litke, A.V. Rudakova, V.K. Ryabchuk, N. Serpone, Langmuir 14 (1998) 5011–5022.

[50] J. Tauc, in: F. Abeles (Ed.), Optical Properties of Solids, North Holland Publishers, Amsterdam, 1970.

[51] G. Blasse, Chem. Phys. Lett. 20 (1973) 573–574.

[52] R. Reisfeld, E. Zigansky, M. Gaft, Mol. Phys. 102 (2004) 1319–1330.

[53] P.K. Sharma, R. Nass, H. Schmidt, Opt. Mater. 10 (1998) 161–169.

[54] R. Gunawidjaja, T. Myint, H. Eilers, Chem. Phys. Lett. 515 (2011) 122–126.

[55] C. Li, G. Fang, Q. Fu, F. Su, G. Li, X.Z. Wu, X. Zhao, J. Cryst. Growth 292 (2006) 19–24.

[56] X.Y. Chen, G.K. Liu, J. Solid State Chem. 178 (2005) 419–428.

[57] Z. Wei, L. Sun, C. Liao, J. Yin, X. Jiang, C. Yan, S. Lu, J. Phys. Chem. B 106 (2002) 10610–10617.

[58] N. Dhananjaya, H. Nagabhushana, B.M. Nagabhushana, B. Rudraswamy, C. Shivakumara, K. Narahari, R.P.S. Chakradhar, Spectrochim. Acta, Part A 86 (2012) 8–14.

[59] F. Wang, X.G. Liu, Chem. Soc. Rev. 38 (2009) 976–989.

[60] T. Nianjbadgar, G. Garnweitner, A. Borger, L.M. Goldenberg, O.V. Sakhno, J. Stumpe, Adv. Funct. Mater. 19 (2009) 1819–1825.

[61] G. Blasse, Philips Res. Rep. 24 (1969) 131–144.

[62] L.G.V. Uitert, J. Electrochem. Soc. 114 (1967) 1048–1053.

[63] R. Naik, S.C. Prashantha, H. Nagabhushana, S.C. Sharma, B.M. Nagabhushana, H.P. Nagaswarupa, H.B. Premkumar, Sens. Actuators, B 195 (2014) 140–149.